

Article

# Frequency Tuning in Inductive Power Transfer Systems

Manuele Bertoluzzo \* and Giuseppe Buja 

Department of Industrial Engineering, University of Padova, 35131 Padova, Italy; giuseppe.buja@unipd.it

\* Correspondence: manuele.bertoluzzo@unipd.it; Tel.: +39-049-827-7923

Received: 21 February 2020; Accepted: 21 March 2020; Published: 23 March 2020



**Abstract:** Inductive power transfer systems (IPTSs) systems are equipped with compensation networks that resonate at the supply frequency with the inductance of the transmitting and receiving coils to both maximize the power transfer efficiency and reduce the IPTS power sizing. If the network and coil parameters differ from the designed values, the resonance frequencies deviate from the supply frequency, thus reducing the IPTS efficiency. To cope with this issue, two methods of tuning the IPTS supply frequency are presented and discussed. One method is aimed at making resonant the impedance seen by the IPTS power supply, the other one at making resonant the impedance of the receiving stage. The paper closes by implementing the first method in an experimental setup and by testing its tuning capabilities on a prototypal IPTS used for charging the battery of an electric vehicle.

**Keywords:** inductive power transfer systems; compensation networks; supply frequency tuning

## 1. Introduction

Inductive power transfer (IPT) is a viable technology that allows getting rid of any grid connection while charging the battery of a mobile equipment, including electric vehicles (EVs) [1,2]. Specifically, commercial IPT systems (IPTSs) that transfer few kW for the charge of parked EVs are available on the market [3,4], while prototypal IPTSs of tens of kW have been recently assembled [5–7].

The core of an IPTS is the coupler; it is made of two coils, one placed in the receiving stage and the other one in the transmitting stage. An inverter operating at high frequency (HF) supplies the transmitting coil that, thanks to the coupling, induces a voltage across the receiving coil. The induced voltage, after being properly conditioned, charges the battery.

To enhance one or more features of the IPTS, such as efficiency of the power transfer, power sizing of the inverter and sensitivity against coils misalignment, compensation networks made of reactive elements are inserted in both transmitting and receiving stages. The reactive elements are typically sized to achieve some form of resonance with the coil's inductances at the supply frequency [8]. This paper is concerned with such an issue for IPTSs compensated by inserting a capacitor in series to each coil.

The drift of the IPTS' reactive elements (coils and networks components) and manufacturing tolerances can deviate the resonance frequency of the stages from the supply frequency, thus affecting the performance of the IPTS. Some papers studied how the loss of resonance affects the output power of the system [9] and other considered also its effects on the efficiency [10], but they did not propose countermeasures aimed to regain a satisfactory level of efficiency. In literature, two approaches to resonance restoration are found: some authors keep the supply frequency constant and act on the reactive parameters of the coils or of the compensation networks to achieve the resonance [11–13]; other authors, instead, adjust the supply frequency to reach a given performance index [14–17]. In paper [11] an additional coil, coupled with the receiving one, is suitably fed in order to induce across the latter one a voltage that changes its equivalent reactance with the aim of maximizing the voltage applied to

the equivalent load. In [12] the inductance of the transmitting coil is adjusted by varying the saturation level of its core; to this end, a controlled DC current is injected in an additional coil wounded on the same core. The solution presented in [13] provides for several additional capacitors that can be selectively connected by electronic switches in parallel to main compensation capacitor to achieve the resonance condition at the transmitting side. With respect to the above-cited solutions, the presented one does not require any additional coil or capacitor to achieve the resonance and leads to a much simpler implementation of the IPTS.

Paper [14] follows the approach of varying the supply frequency. The authors propose to perform a sweep of the supply frequency from the minimum to the maximum to find which one gives the maximum output voltage and considers it as the resonance frequency; after this adjustment, the frequency is kept constant and no real time tuning is performed. In [15] a closed loop control of the amplitude of the current in the transmitting coil is implemented; it uses as reference the amplitude that theoretically should be achieved in resonance condition and as manipulated variable the supply frequency. A real time closed loop approach is applied also in [16], which considers an RF IPTS whose supply frequency spans from 40 MHz to 120 MHz and is adjusted in order to minimize the fraction of the RF signal reflected from the transmitter. Paper [17] reports a tuning method like one of the two methods dealt with in the presented paper. This paper, however, offers much more detailed insights both from the theoretical and the experimental points of view, together with the opportunity of comparing the performance of two different tuning method applied to the same IPTS, and takes into consideration the bifurcation phenomenon, not mentioned in any of the cited papers. More in detail, differently from [14], the tuning method implemented in the prototype does not require transferring any information from the receiving to the transmitting stage of the IPTS, thus greatly simplifying its implementation, and differently from [15], the resonance condition is recognized elaborating real time data instead of relaying in theoretical relations. Moreover, the frequency tuning is completely independent from voltage or current control, so that a much higher flexibility in the management of the IPTS is preserved.

The paper is organized as follows. After reviewing the IPTS equations under ideal resonance operation, the impact on the efficiency of the variations of the reactive elements is analyzed. Then, the two methods of tuning the supply frequency are examined and a control system is arranged to execute the tuning task. Specifically, the first method forces to zero the phase angle between the fundamental voltage component at the output of the HF inverter to the current flowing through it. The second method forces to zero the phase angle between the voltage induced in the receiving coil and the current flowing through it. Characteristics of the two methods are investigated, emerging that they differ in sensitivity to the bifurcation phenomenon [18,19]. Lastly, implementation of the first method in a setup committed to the adjustment of the supply frequency of a prototypal IPTS is described and the results of experimental tests corroborating the tuning capabilities of the method are given.

## 2. Background

Compensation networks composed of one or more reactive components and arranged according to several topologies have been proposed in the literature for the IPTSs [20–22]. The simplest compensation network uses a capacitor for each IPTS coil with either a series or parallel connection. The most straightforward topology is the series-series (SS) one, with the capacitors connected in series to the coils and resonating with them at the supply frequency. The SS topology is taken as the study-case in this paper because it is largely used for its good performance in terms of efficiency and sizing power of the IPTSs [23]. This topology makes the resonance condition of the IPTS insensitive to the coil misalignment, thus the issues arising from misalignment are not considered in designing the tuning methods. This approach does not limit the field of application of the proposed solution because recent EVs are equipped with parking systems that, either automatically or assisting the driver, could reduce the misalignment near to zero.

The scheme of an SS-compensated IPTS is illustrated in Figure 1, where the coil inductance of the transmitting stage is designated with  $L_T$ , the current flowing through it with  $i_T$ , the in-series capacitance with  $C_T$ , and the parasitic coil resistance with  $r_T$ ; the corresponding quantities in the receiving stage are designated with  $L_R$ ,  $i_R$ ,  $C_R$ , and  $r_R$ . The transmitting stage includes the IPTS power supply; it consists of an HF inverter fed by DC voltage source  $V_{DC,T}$  and generating square-wave voltage  $v_S$ ; due to the HF operation of the inverter, voltage  $v_S$  is commonly adjusted by the phase shift technique. The IPTS coupler is represented by mutual inductance  $M$  and induced voltages  $v_T$  and  $v_R$ . The receiving stage also contains a diode rectifier (DR) with capacitor  $C_L$  levelling the DR output voltage at  $V_{DC,R}$  and a buck chopper (CH) that provides for charging the battery with the required current profile. Since current  $i_R$  entering the DR flows along the whole supply period, the DR conduction is continuous. Therefore, voltage  $v_L$  at the DR input is a square-wave of magnitude  $V_{DC,R}$ . Series resonance in both IPTS stages is obtained by sizing the series capacitors according to

$$C_T = \frac{1}{\omega^2 L_T}; C_R = \frac{1}{\omega^2 L_R} \tag{1}$$

where  $\omega$  is the IPTS supply angular frequency. Resonance makes currents  $i_T$  and  $i_R$  nearly sinusoidal despite the square waveform of voltages  $v_S$  and  $v_L$ . Consequently, only their fundamental component takes part in the power transfer from the inverter output to the DR input, and the scheme of Figure 1 can be represented with the circuit of Figure 2. In the figure, voltages  $v_S$  and  $v_L$  are substituted for by their first harmonics  $v_{S,1}$  and  $v_{L,1}$ , respectively. Moreover, since currents and voltages in the circuit are sinusoidal, they are expressed by phasors and are denoted by upper-case letters overmarked with a bar while their magnitudes are denoted by capital letters. The impedances, like  $\dot{Z}_{ref}$ , are denoted by upper-case letters overmarked with a point.

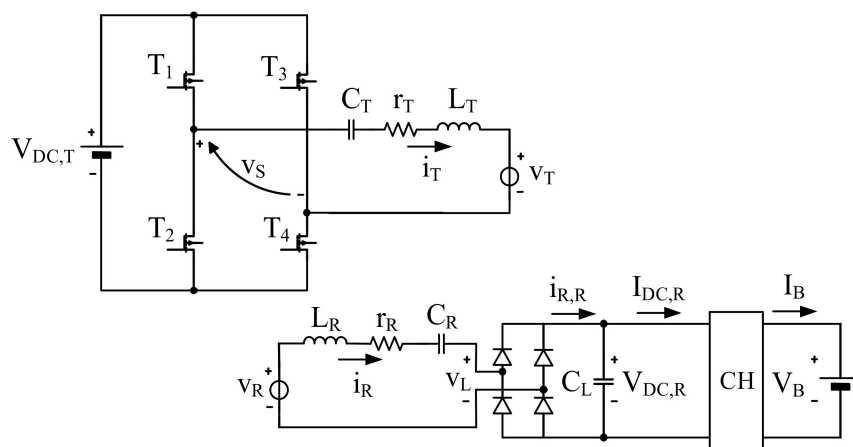


Figure 1. Scheme of SS-compensated IPTS.

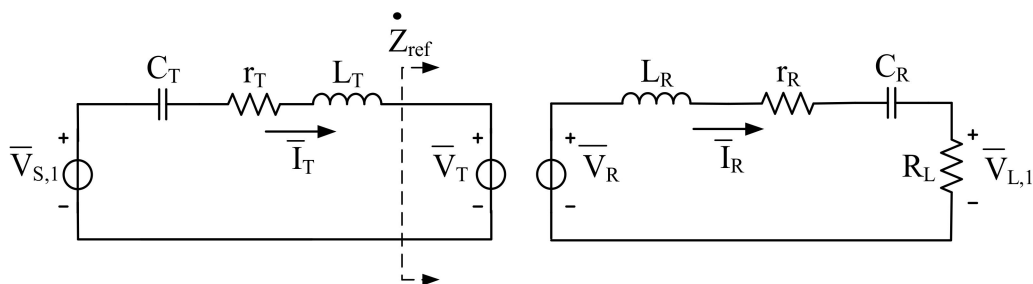


Figure 2. Circuitual representation of SS-compensated IPTS.

Resistor  $R_L$  is the IPTS load, given by the equivalent resistance of the cascade of DR, CH, and battery. It is obtained considering at first the equivalent resistance  $R_B$  of the battery, defined as the ratio  $V_B/I_B$  of the battery voltage to the charging current. The resistance seen at the CH input is then

$$R_{CH} = \frac{1}{\delta^2} R_B \tag{2}$$

where  $\delta$  is the chopper duty-cycle. Resistance  $R_{CH}$  is also defined as the ratio  $V_{DC,R}/I_{DC,R}$ , where  $I_{DC,R}$  is the average value of  $i_{R,R}$ , which is obtained by rectification of  $i_R$ . On its turn,  $R_L$  is defined as  $V_{L,1}/I_R$  where  $V_{L,1}$  and  $I_R$  are the magnitudes of  $v_{L,1}$  and  $i_R$ , respectively. From these equalities, it follows that

$$R_L \triangleq \frac{V_{L,1}}{I_R} = \frac{\frac{4}{\pi} V_{DC,R}}{\frac{\pi}{2} I_{DC,R}} = \frac{8}{\pi^2} R_{CH} \tag{3}$$

Impedance  $\dot{Z}_{ref}$  in Figure 2 is the receiving stage impedance reflected to the transmitting stage. Other impedances of interest of the circuit are  $\dot{Z}_T$  and  $\dot{Z}_R$ , i.e., the impedances of the transmitting and receiving stages, given by

$$\begin{cases} \dot{Z}_T = j\omega L_T + \frac{1}{j\omega C_T} + r_T \\ \dot{Z}_R = j\omega L_R + \frac{1}{j\omega C_R} + r_R + R_L \end{cases} \tag{4}$$

By Figure 2, current  $\bar{I}_T$  is related to  $\bar{V}_{S,1}$  by

$$\bar{V}_{S,1} = (\dot{Z}_T + \dot{Z}_{ref}) \bar{I}_T \tag{5}$$

and  $\bar{I}_R$  to  $\bar{V}_R$  by

$$\bar{V}_R = \dot{Z}_R \bar{I}_R. \tag{6}$$

As a function of the circuitry parameters, impedance  $\dot{Z}_{ref}$  is expressed as

$$\dot{Z}_{ref} = \frac{\omega^2 M^2}{\dot{Z}_R} = \frac{\omega^2 M^2}{j\omega L_R + \frac{1}{j\omega C_R} + r_R + R_L}. \tag{7}$$

By definition, IPTS efficiency is

$$\eta \triangleq \frac{P_L}{P_S} = \frac{R_L |\bar{I}_R|^2 / 2}{\Re[\bar{V}_{S,1} \bar{I}_T^*] / 2} = \frac{R_L \omega^2 M^2}{|\dot{Z}_R|^2 \Re[\dot{Z}_T] + \omega^2 M^2 \Re[\dot{Z}_R]}, \tag{8}$$

where  $P_L$  is the active power drawn by the load,  $P_S$  is the active power delivered by the inverter, and operator  $\Re[\cdot]$  gives the real part of its argument.

### 3. Resonance Operation

Under IPTS ideally resonant operation, resonance angular frequencies  $\omega_T$  and  $\omega_R$  of the transmitting and receiving stages coincide, and the IPTS supply angular frequency  $\omega$  is equal to them. By designating with  $\omega_0$  the common operation angular frequency, it is

$$\omega_T = \frac{1}{\sqrt{L_T C_T}}; \omega_R = \frac{1}{\sqrt{L_R C_R}}; \omega_T = \omega_R \triangleq \omega_0; \omega = \omega_0. \tag{9}$$

Substituting (9) into (4), impedances  $\dot{Z}_T$  and  $\dot{Z}_R$  are found to be purely resistive and equal to

$$\begin{cases} \dot{Z}_T = r_T \\ \dot{Z}_R = r_R + R_L \end{cases} \quad (10)$$

so that (5) and (6) are simplified into

$$\bar{V}_{S,1} = \left( r_T + \frac{\omega_0^2 M^2}{r_R + R_L} \right) \bar{I}_T \quad (11)$$

$$\bar{V}_R = (r_R + R_L) \bar{I}_R. \quad (12)$$

Equations (11) and (12) point out that the following conditions hold when (9) is satisfied:

- C1) voltage  $v_{S,1}$  is in phase to  $i_T$ ,
- C2) voltage  $v_R$  is in phase to  $i_R$ .

Substitution of (10) into (8) leads to the expression of the IPTS efficiency under ideally resonant operation, given by

$$\eta_{rc} = \frac{R_L \omega_0^2 M^2}{(r_R + R_L) [r_T (r_R + R_L) + \omega_0^2 M^2]}. \quad (13)$$

By derivation of (13) with respect to  $\omega_0$ , the following threshold value for  $R_L$  is found:

$$R_{L,th} = \sqrt{\frac{2L_R}{C_R}} - r_R \quad (14)$$

such that:

- i) if  $R_L < R_{L,th}$ , efficiency  $\eta_{rc}$  gets the maximum value of

$$\eta_{rc,max} = \frac{R_{L,th} \omega_{max}^2 M^2}{(r_R + R_{L,th}) [r_T (r_R + R_{L,th}) + \omega_{max}^2 M^2]} \quad (15)$$

for  $\omega$  equal to

$$\omega_{max} = \omega_0 \sqrt{\frac{1}{1 - \left(\frac{R_L}{R_{L,th}}\right)^2}}. \quad (16)$$

From (13)–(16), it follows that a)  $\eta_{rc,max}$  is reached for a supply angular frequency a little higher than  $\omega_0$ , and b)  $\eta_{rc}$  stays close to  $\eta_{rc,max}$  when  $R_L$  varies, provided that it remains less than  $R_{L,th}$ ,

- ii) if  $R_L > R_{L,th}$ , efficiency  $\eta_{rc}$  does not get a maximum but is an increasing function of  $\omega_0$ .

#### 4. Frequency Tuning

The actual values of the IPTS reactive elements may differ from the designed ones at the assembly time, because of the manufacturing tolerances, as well as during the operating life because of the drift due, for instance, to their ageing. This gives rise to a frequency mismatch in (9) and IPTS ideal resonant operation is lost in the transmitting and/or receiving stage.

Impact of a frequency mismatch on the IPTS efficiency is exemplified in Figure 3 for a prototypal IPTS used to charge a city-car EV; the designed values of its reactive elements and the supply frequency are listed in Table 1 together with the load in nominal battery charging conditions [24].

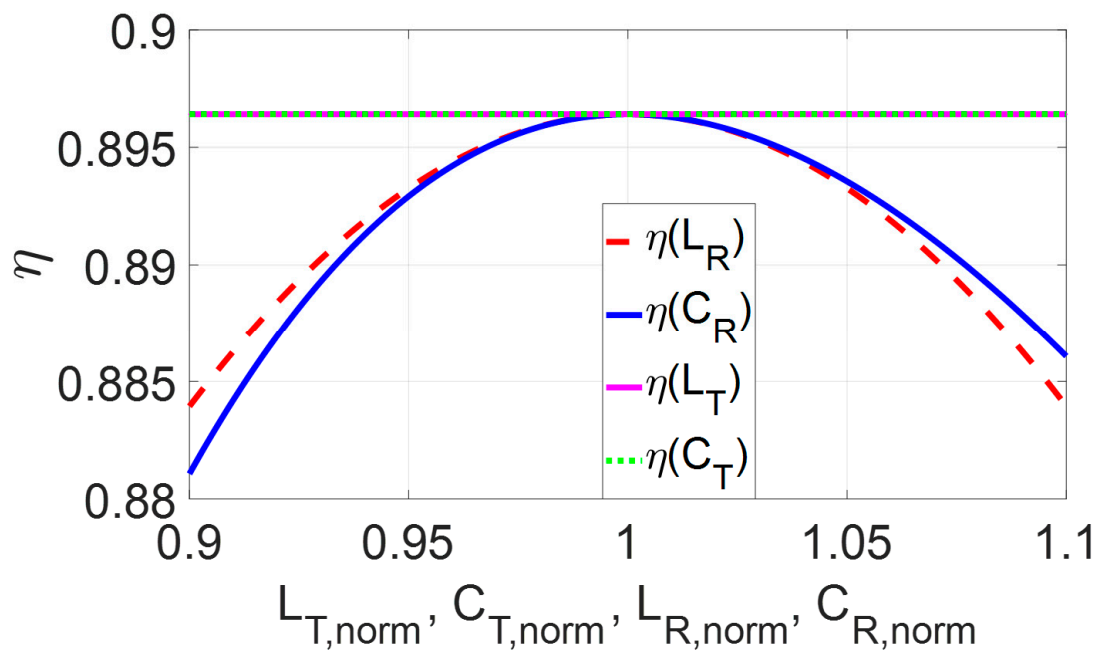


**Figure 3.** Efficiency under IPTS non-ideal resonant operation due to variation of the reactance of the coils or of the resonant capacitors.

**Table 1.** IPTS parameter designed values.

Parameter	Symbol	Designed Value
IPTS supply frequency	$f$	85 kHz
Coupling coil inductances	$L_T, L_R$	120 $\mu\text{H}$
Resonant capacitances	$C_T, C_R$	29.2 nF
Series resistances	$r_T, r_R$	0.6 $\Omega$
Mutual inductance	$M$	30 $\mu\text{H}$
Load	$R_L$	6.1 $\Omega$

The figure plots four graphs of efficiency, calculated from (8) by varying one at a time  $L_T$ ,  $C_T$ ,  $L_R$  and  $C_R$  and by setting  $\omega$  at  $\omega_0$ . In the graphs, the values of the reactive elements range from  $-10\%$  to  $+10\%$  of their designed values. For the sake of completeness, Figure 4 plots the graph of efficiency for the reactive elements set at the designed values and for  $\omega$  varying in the range 81.38 kHz  $\div$  90 kHz. The selected  $\omega$  range follows that set by SAE (Society of Automotive Engineers) RP (Recommended Practice) J2954 for IPTSs projected to charge the battery of EVs. In all graphs, the x-axis is normalized to the design value of the relevant quantity. Inspection of Figure 3 reveals that the impact of  $L_R$  and  $C_R$  variations, plotted respectively with the red dashed line and the blue solid line, is nearly the same and reduces the efficiency of more than 1% in the worst case. Instead, the  $L_T$  and  $C_T$  variations, plotted respectively with the horizontal magenta and green dotted lines, do not have any effect on the efficiency. The last outcome is a consequence of (8), where only the real part of  $\dot{Z}_T$  appears in the expression of the efficiency. Regarding the impact of the  $\omega$  variations on the efficiency, Figure 4 reveals that the efficiency decreases of about 0.5% at the ends of the spanned  $\omega$  range and gets its maximum for a  $\omega_{\text{norm}}$  value a little bigger than 1, in agreement with (16).

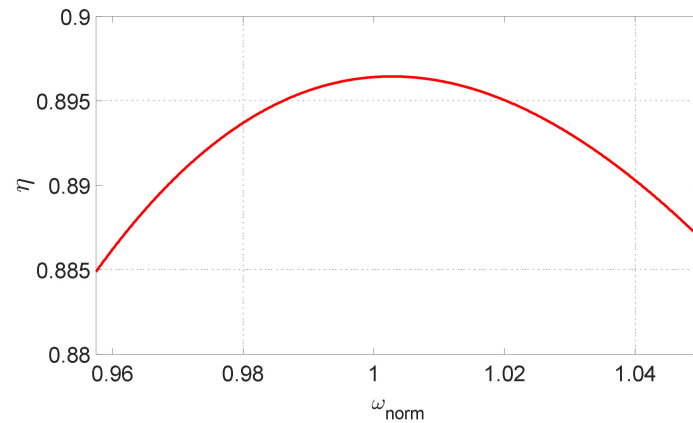


**Figure 4.** Efficiency under IPTS non-ideal resonant operation due to variation of the supply angular frequency.

Resonance operation can be enforced by tuning the supply frequency but the IPTS ideally resonant operation cannot be reached because, in general, the resonance frequencies of the two stages do not deviate of an equal value. By accounting of the IPTS quantities that can be practically sensed, two tuning methods are envisaged. The first method tunes the supply frequency to make resonant the impedance seen from the inverter output and is hereafter termed as transmitting side resonance (TSR) method. The second one tunes the supply frequency to make resonant the receiving stage, i.e., it sets  $\omega$  at  $\omega_R$ , and is hereafter termed as the receiving side resonance (RSR) method.

#### 4.1. TSR Method

The condition to achieve TSR is defined as C1) in Section 3. By (11), the requirement of having  $v_{S,1}$  in phase to  $i_T$  is equivalent to

$$\Im[\dot{Z}_T + \dot{Z}_{ref}] = 0 \tag{17}$$

where  $\Im[\cdot]$  is the operator that returns the imaginary part of its argument. By (6) and (7), relation (17) is rewritten in the following polynomial form:

$$P(u) \equiv A_3u^3 + A_2u^2 + A_1u + A_0 = 0 \tag{18}$$

where  $\omega^2$  had been replaced with  $u$  and coefficients  $A_3$ ,  $A_2$ ,  $A_1$  and  $A_0$  are

$$\begin{cases} A_3 = C_T L_R C_R^2 (L_T L_R - M^2) \\ A_2 = -2L_T C_T L_R C_R - L_R^2 C_R^2 + L_T C_T C_R^2 (r_R + R_L)^2 + C_T C_R M^2 \\ A_1 = L_T C_T + 2L_R C_R - C_R^2 (r_R + R_L)^2 \\ A_0 = -1 \end{cases} \tag{19}$$

Polynomial  $P(u)$  is of third degree and all its coefficients are real. Consequently,  $P(u)$  has at least one real solution  $u_1$ . Being  $A_3 > 0$  and  $A_0 < 0$ ,  $u_1$  is positive and a supply angular frequency, denoted with  $\omega_{TSR,1} = \sqrt{u_1}$ , exists that forces  $i_T$  in phase to  $v_{S,1}$ . Moreover,  $P(u)$  has other two solutions that if real and positive, give rise to two additional supply angular frequencies that forces  $i_T$  in phase to  $v_{S,1}$ , originating the phenomenon known as bifurcation. On the chance that  $\omega_T = \omega_R$ , paper [25] has set forth the constraints by which the other two solutions are real and positive. Instead, for  $\omega_T \neq \omega_R$ , the constraints can be found by the Descartes rule of signs. The rule states that if a polynomial has real coefficients and they are sorted by the descending order of the exponent, the number of the real and positive roots is either equal to the number of sign changes between consecutive coefficients or is

lower than it by an even number. For  $P(u)$  in (18), the other two solutions can exist only if  $A_2 < 0$  and  $A_1 > 0$ . Constraint  $A_1 > 0$  requires that

$$R_L < R_{L,B1} \triangleq \sqrt{\frac{2L_R}{C_R} + \frac{L_T C_T}{C_R^2}} - r_R \tag{20}$$

while constraint  $A_2 < 0$  requires that

$$R_L < R_{L,B2} \triangleq \sqrt{\frac{2L_R}{C_R} + \frac{L_R^2}{L_T C_T} - \frac{M^2}{L_T C_R}} - r_R. \tag{21}$$

Fulfillment of the constraints is a necessary but not sufficient condition to have bifurcation. However, it can be asserted that i) at low power, i.e., for high values of  $R_L$ , IPTS is likely free from bifurcation, and ii) as the power increases, IPTS could be subjected to bifurcation.

Comparison of (20) with (14) reveals that  $R_{L,th}$  is always lower than  $R_{L,B1}$  while it is lower than  $R_{L,B2}$  only if

$$1 - k^2 \frac{L_T C_T}{L_R C_R} > 0 \tag{22}$$

where  $k$  is the coupling coefficient of the coupler. Because of the low values taken by  $k$  in IPTSs, inequality (22) is verified unless the difference between the designed and actual values of the reactive elements gets very high.

Improvement in the efficiency attained with the TSR method has been examined for the prototypal IPTS by taking as supply angular frequency the central solution of (18) whenever bifurcation is detected. The results are plotted in Figure 5 with the same conventions as used in Figure 3. Inspection of the figure outlines that the graphs relevant to the pair  $L_T, C_T$  are nearly superimposed such as in Figure 3, but now the same happens also for the pair  $L_R, C_R$ . Moreover, the graphs show that efficiency is near to that of IPTS under ideally resonant operation, or even higher when either  $L_R$  or  $C_R$  goes below their designed values. Instead, a small reduction of the efficiency happens when the loss of resonance is caused by variations of  $L_T$  or  $C_T$ .

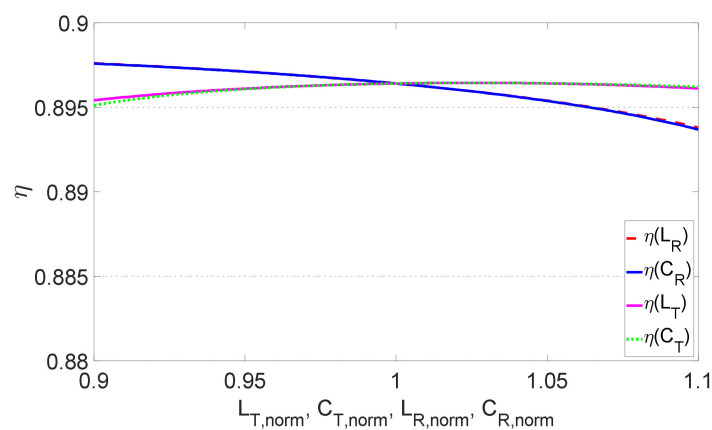


Figure 5. Efficiency improvement by TSR method.

#### 4.2. RSR Method

The condition to achieve RSR is defined as C2) in Section 3. By (5), the requirement of having  $v_R$  in phase to  $i_R$  is equivalent to

$$\Im[\dot{Z}_R] = 0. \tag{23}$$

Differently from the TSR method, relation (23) leads to an equation that has always one and only one positive solution, given by

$$\omega_{RSR} = \omega_R = \frac{1}{\sqrt{L_R C_R}} \tag{24}$$

Improvement in the efficiency attained with this tuning method is plotted in Figure 6. The graphs underline that the improvement is like the TSR method when  $L_R$  and  $C_R$  go lower than the designed values, and even better when they go higher. As (24) is not affected by  $L_T$  and  $C_T$ , the efficiency remains constant despite the variations of these reactive elements.

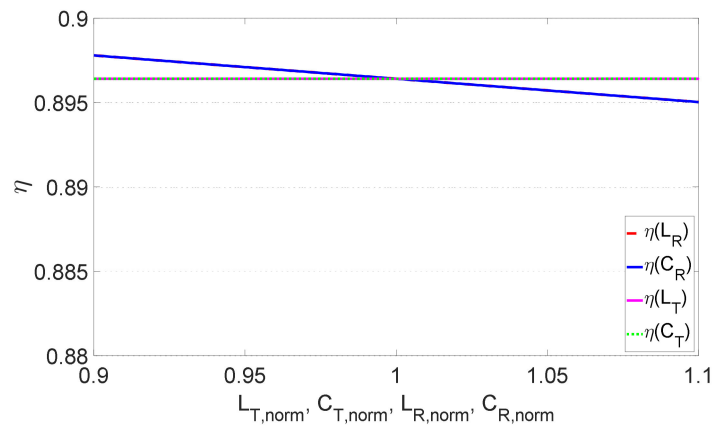


Figure 6. Efficiency improvement by RSR method.

### 5. Phase Control System

Implementation of either of the two methods calls for a phase control system that, acting on the IPTS supply frequency, drives to zero the phase between  $v_{S,1}$  and  $i_T$ , for the TSR method, and the phase between  $v_R$  and  $i_R$ , for the RSR method. Regarding the implementation of the latter method, it is worth noting that  $v_R$  cannot be transduced directly from the terminals of the receiving coil because the voltage between them is comprehensive of the voltage drop across  $L_R$ . However, being  $v_R$  related to  $i_T$  by

$$\bar{V}_R = -j\omega M \bar{I}_T \tag{25}$$

the RSR method is implemented equally well by forcing  $i_T$  to lead  $i_R$  of  $\pi/2$ .

#### 5.1. Phase Control

The cumulative block diagram of the phase control system for the two methods is shown in Figure 7. In the diagram, the solid-line paths and the variables with no brackets pertain to the block diagram of both TSR and RSR methods. Instead, variables within curly brackets are relevant to the TSR method while those within the square ones to the RSR method.

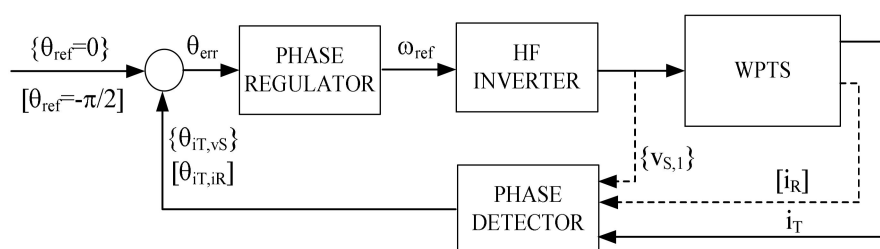


Figure 7. Block diagram of the phase control system.

Phase error  $\theta_{err}$  in the diagram is the difference of phase angle reference  $\theta_{ref}$  to the actual value  $\theta_{act}$  of the controlled phase angle. For the TSR method,  $\theta_{ref}$  is equal to zero and  $\theta_{act}$  is the phase angle

$\theta_{i_T, v_S}$  between  $i_T$  and  $v_S$ ; for the RSR method,  $\theta_{ref}$  is equal to  $-\pi/2$  and  $\theta_{act}$  is the phase angle  $\theta_{i_T, i_R}$  between  $i_T$  and  $i_R$ . The phase regulator manipulates  $\theta_{err}$  and generates reference  $\omega_{ref}$  of the IPTS supply angular frequency, which is impressed by the inverter. To protect the phase control system from large errors, phase error  $\theta_{err}$  is clamped at  $[-30^\circ, 30^\circ]$  before being entered into the regulator.

### 5.2. Phase Regulator

Specifications for the phase control system are zero phase error at steady state and a reasonably damped behavior. At steady state, the phase relation between the transduced signals depends only on the actual value of  $\omega$ ; hence, the phase regulator must execute an integral action on  $\theta_{err}$  for it to reach zero.

By (4), (6) and (7), the phase relations between  $i_T$  and  $v_{s,1}$  at very high and very low supply angular frequency are

$$\left\{ \begin{array}{l} \left. \frac{\bar{V}_{S,1}}{\bar{I}_T} \right|_{\omega \rightarrow \infty} \cong j\omega L_T \left(1 - \frac{M^2}{L_T L_R}\right) \Rightarrow \lim_{\omega \rightarrow \infty} \theta_{i_T, v_S} = -\frac{\pi}{2} \\ \left. \frac{\bar{V}_{S,1}}{\bar{I}_T} \right|_{\omega \rightarrow 0} \cong \frac{1}{j\omega C_T} \Rightarrow \lim_{\omega \rightarrow 0} \theta_{i_T, v_S} = \frac{\pi}{2} \end{array} \right. \quad (26)$$

By (4), (6) and (25), the phase relations between  $i_T$  and  $i_R$  under the same situations are

$$\left\{ \begin{array}{l} \left. \frac{\bar{I}_R}{\bar{I}_T} \right|_{\omega \rightarrow \infty} \cong -\frac{M}{L_R} \Rightarrow \lim_{\omega \rightarrow \infty} \theta_{i_T, i_R} = -\pi \\ \left. \frac{\bar{I}_R}{\bar{I}_T} \right|_{\omega \rightarrow 0} \cong \frac{1}{\omega^2 M C_R} \Rightarrow \lim_{\omega \rightarrow 0} \theta_{i_T, i_R} = 0 \end{array} \right. \quad (27)$$

For the TSR method, when (18) has only one solution,  $\theta_{i_T, v_S}$  decreases with  $\omega$  and the gain of the phase regulator must be negative; if bifurcation occurs, an interval of  $\omega$  exists where  $\theta_{i_T, v_S}$  increases with  $\omega$  and the gain of the phase regulator must be positive. It follows that the phase regulator must be able to recognize the correct sign for its gain. For the RSR method, this problem does not exist because  $\theta_{i_T, i_R}$  is always a decreasing function of  $\omega$  and the gain of the phase regulator must be negative.

To comply with the issues of the TSR method, a phase regulator has been synthesized, committed with the task of checking at the beginning of each sampling period if the actual absolute value of the phase error is smaller or greater than that one in the previous sampling period. In the first case, the sign of the gain is maintained while in the second case it is changed before updating  $\omega_{ref}$ .

## 6. Experimental Results

### 6.1. Experimental Setup

A setup of the phase control system has been arranged according to the TSR method and implemented in the development kit CY8CKIT-059 hosting a programmable system on chip PSoC 5 LC [26], both of Cypress Semiconductor. The setup has been used to tune the supply frequency of the prototypal IPTS pictured in Figure 8. The coupler of the setup is formed by two equal coils that are enclosed in the red plates at the rightmost side of Figure 8. The coils have been designed according to the procedure reported in [27] and have the structure shown in Figure 9. The inverter is built up with a Wolfspeed CCS050M12CM2 SiC MOSFET module [28] and the load is built up with an adjustable resistor emulating a battery with nominal power of 560 W. The PSoC generates the signals to command the inverter switches and a signal proportional to phase error  $\theta_{err}$  through an embedded analog-to-digital converter. Quantities  $v_S$  and  $i_T$ , and the signal proportional to  $\theta_{err}$  are acquired by a Tektronix TDS 5034 digital oscilloscope.

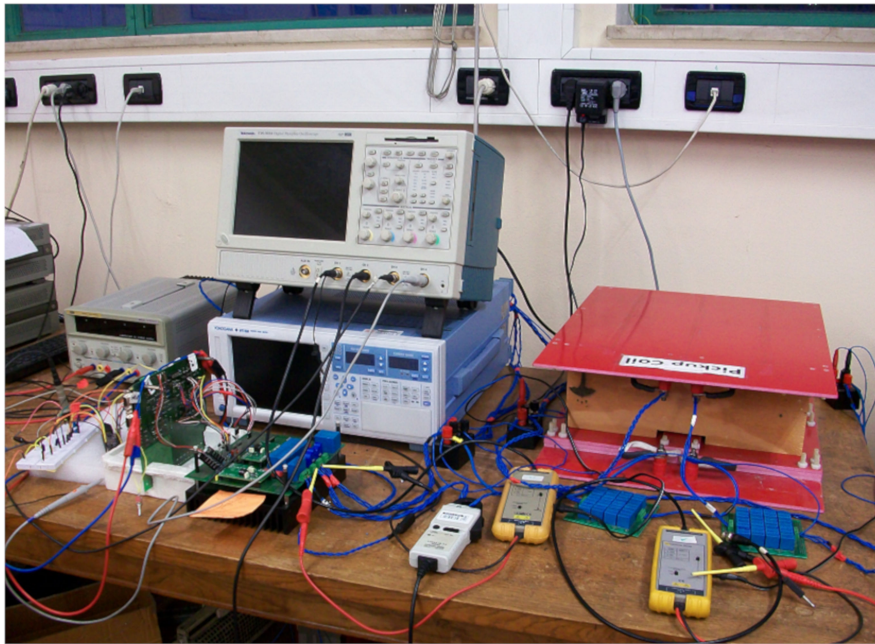


**Figure 8.** Phase control system setup and prototypal IPTS.



**Figure 9.** Coil without protective cover.

## 6.2. Test Results

The phase control system has been subjected to several tests with different IPTS loads and initial supply frequencies to assess its capabilities in reaching the tuning conditions. In the tests, the magnitude of the inverter output voltage has been kept fixed while its frequency has been changed as dictated by the phase control system. Below, two tests carried out with values of  $R_L$  equal to  $5.6 \Omega$  and  $45 \Omega$  are documented; these  $R_L$  values are significant in evaluating the tuning capabilities of the phase control system as the former value does not give rise to any bifurcation while the latter one does it.

The actual values of the reactive elements of the prototypal IPTS have been measured with an Instek LCR meter model LCR-819 and the resulting values are reported in Table 2, together with the coils distance and the  $R_L$  values in (14), (20) and (21). By substituting these values in the first of (4) and (7), phase  $\theta_{i_T, v_S}$  between  $i_T$  and  $v_S$  and ratio (28) have been plotted as a function of  $\omega_{norm}$  respectively

in the upper half and the lower half of Figure 10. Solid and dashed lines in the figure refer respectively to  $R_L$  equal to  $5.6 \Omega$  and  $45 \Omega$ .

$$\frac{|\bar{i}_T|}{|\bar{v}_{S,1}|} = \frac{1}{|\dot{Z}_T + \dot{Z}_{ref}|} \tag{28}$$

**Table 2.** IPTS parameter actual values.

Parameter	Transmitting Side	Receiving Side
	Actual value	Actual value
Coil inductance	122 $\mu$ H	119 $\mu$ H
Resonant capacitance	30.8 nF	30.8 nF
Series resistance	0.7 $\Omega$	0.7 $\Omega$
Mutual inductance	29.5 $\mu$ H	
Coil distance	0.14 m	
	Symbol	Value
$R_L$ from (14)	$R_{L,th}$	87.2 $\Omega$
$R_L$ from (22)	$R_{L,B1}$	107.4 $\Omega$
$R_L$ from (23)	$R_{L,B2}$	105.4 $\Omega$

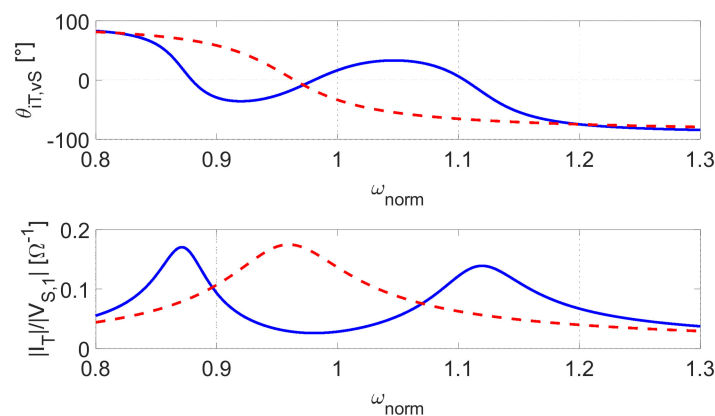


**Figure 10.** Phase angle  $\theta_{iT,vS}$  (up) and ratio  $|\bar{i}_T|/|\bar{v}_{S,1}|$  (down) vs.  $\omega_{norm}$  for  $R_L = 5.6 \Omega$  (blue solid line) and  $R_L = 45 \Omega$  (red dashed line).

In the test with  $R_L = 5.6 \Omega$ , the initial supply frequency is set at 89 kHz, i.e., at  $\omega_{norm} = 1.049$ , and the corresponding waveforms of  $v_S$  and  $i_T$  are plotted in the upper half of Figure 11. Processing of the waveforms has resulted in a value of  $\theta_{iT,v}$  equal to  $27.5^\circ$ . The waveforms of  $v_S$  and  $i_T$  at the completion of the tuning process are plotted in the lower half of Figure 11, and the resultant values of  $\omega_{norm}$  and  $\theta_{iT,vS}$  are 0.997 and  $7.7^\circ$ , respectively. Comparison of the graphs in the two halves of Figure 10 shows that the magnitude of  $i_T$  is lower after tuning, although  $v_{s,1}$  is kept constant. This outcome is substantiated by the solid-line graph in the lower half of Figure 11, which highlights a decrease of  $|\bar{i}_T|/|\bar{v}_{S,1}|$  for  $\omega_{norm}$  moving leftward from the initial value of 1.049.

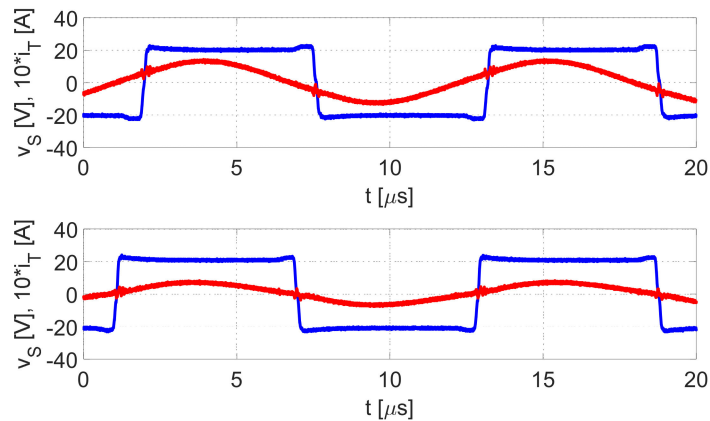


**Figure 11.** Inverter output voltage (blue line) and current (red line) before (up) and after (down) tuning with  $R_L = 5.6 \Omega$ .

The behavior of  $i_T$  during the tuning process is plotted in the upper half of Figure 12. The solid blue graph, made of more than 4000 supply periods, does not permit to appreciate the waveform of  $i_T$ , but confirms that its magnitude decreases about exponentially during the tuning process. The lower half of Figure 12 plots the signal proportional to  $\theta_{err}$ . Its behavior shows that the tuning process exhibits a small overshoot and reaches the steady state in about 25 ms.

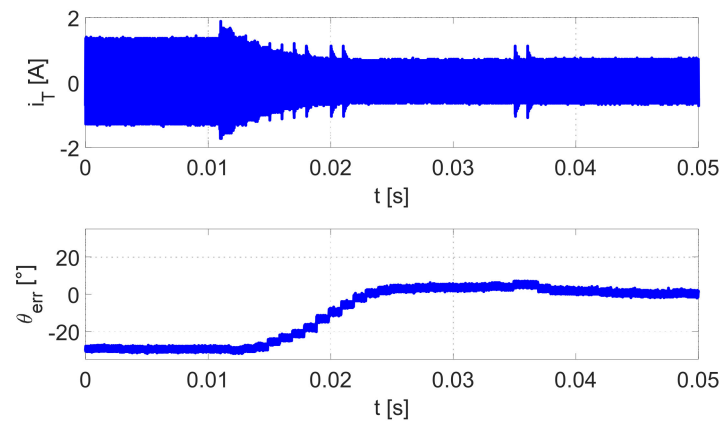


**Figure 12.** Transmitting coil current (up) and phase error (down) during tuning with  $R_L = 5.6 \Omega$ .

The test, repeated with  $R_L = 45 \Omega$ , has led to the graphs in Figures 13 and 14. Now the initial values for  $\omega_{norm}$  and  $\theta_{iT,vS}$  are respectively 1.048 and  $-65.5^\circ$  while, after completion of the tuning process, they are 0.956 and  $-5.6^\circ$ . The graphs show that the magnitude of  $i_T$  increases after tuning; again, this outcome is substantiated by the dashed-line graph of  $|\bar{I}_T|/|\bar{V}_{S,1}|$  in the lower half of Figure 9, which highlights an increase of  $|\bar{I}_T|/|\bar{V}_{S,1}|$  for  $\omega_{norm}$  moving leftward from the initial value of 1.049. Here, the steady state is reached in about 25 ms without any overshoot.

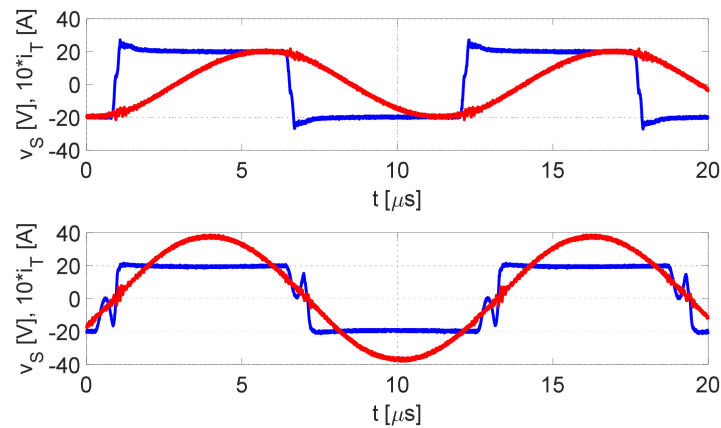


**Figure 13.** Inverter output voltage (blue line) and current (red line) before (up) and after (down) tuning with  $R_L = 45 \Omega$ .

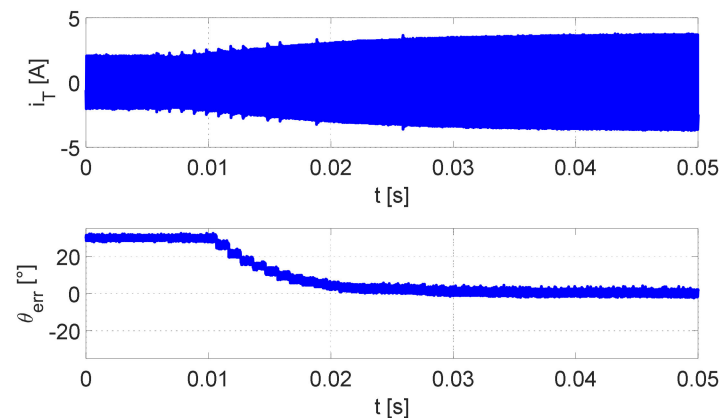


**Figure 14.** Transmitting coil current (up) and phase error (down) during tuning with  $R_L = 45 \Omega$ .

The experimental results demonstrate that the TSR method works correctly both with and without bifurcation occurrence and is effective in reducing the phase error between  $i_T$  and  $v_S$  substantially, even if not exactly to zero. The residual error can be ascribed, at least partially, to the fact that the imposed supply frequency is a submultiple of the clock frequency of PSoC, which does not guarantee the accurate application of the requested frequency.

## 7. Conclusions

The paper has dealt with the tuning of the supply frequency of IPTSs to improve their efficiency in presence of drifts or tolerances of the reactive elements. After reviewing the impact on the efficiency of the loss of resonance, two methods of tuning the IPTS supply frequency have been examined that impose the resonance condition on either the impedance seen by the transmitting side (TSR) or the receiving side impedance (RSR). Examination of the methods has revealed the occurrence of the bifurcation phenomenon in the TSR method. A phase control system that takes over of the tuning process for both methods has been developed. Implementation of the phase control system in a setup intended to tune the supply frequency of a prototypal IPTS according to the TSR method has been illustrated, together with the countermeasures adopted to face up the bifurcation phenomenon. Finally, the results of experimental tests have been reported to illustrate the tuning capabilities of the method.

**Author Contributions:** Conceptualization, M.B. and G.B.; methodology, M.B. and G.B.; software, M.B.; validation, M.B., and G.B.; formal analysis, M.B.; investigation, M.B.; writing—original draft preparation, M.B.; writing—review and editing, G.B. All authors have read and agreed to the published version of the manuscript.

**Funding:** This research received no external funding.

**Conflicts of Interest:** The authors declare no conflict of interest.

## References

1. Zhang, Z.; Pang, H.; Georgiadis, A.; Cecati, C. Wireless Power Transfer—An Overview. *IEEE Trans. on Ind. Electron.* **2019**, *66*, 1011–1058. [[CrossRef](#)]
2. Mi, C.C.; Buja, G.; Choi, S.Y.; Rim, C.T. Modern Advances in Wireless Power Transfer Systems for Roadway Powered Electric Vehicles. *IEEE Trans. Ind. Electron.* **2016**, *63*, 6533–6545. [[CrossRef](#)]
3. Mou, X.; Groling, O.; Sun, H. Energy-Efficient and Adaptive Design for Wireless Power Transfer in Electric Vehicles. *IEEE Trans. Ind. Electron.* **2017**, *64*, 7250–7260. [[CrossRef](#)]
4. Bosshard, R.; Kolar, J.W. Inductive power transfer for electric vehicle charging: Technical challenges and tradeoffs. *IEEE Power Electron. Mag.* **2016**, *3*, 22–30. [[CrossRef](#)]
5. Deng, Q.; Liu, J.; Czarkowski, D.; Hu, W.; Zhou, H. An Inductive Power Transfer System Supplied by a Multiphase Parallel Inverter. *IEEE Trans. Ind. Electron.* **2017**, *64*, 7039–7048. [[CrossRef](#)]
6. Jiang, Y.; Wang, L.; Wang, Y.; Liu, J.; Li, X.; Ning, G. Analysis, design and implementation of accurate ZVS angle control for EV's battery charging in wireless high power transfer. *IEEE Trans. Ind. Electron.* **2019**, *66*, 4075–4085. [[CrossRef](#)]
7. Keeling, N.A.; Covic, G.A.; Boys, J.T. A Unity-Power-Factor IPT Pickup for High-Power Applications. *IEEE Trans. Ind. Electron.* **2010**, *57*, 744–751. [[CrossRef](#)]
8. Kim, J.-G.; Wei, G.; Kim, M.-H.; Jong, J.-Y.; Zhu, C. A Comprehensive Study on Composite Resonant Circuit-Based Wireless Power Transfer Systems. *IEEE Trans. Ind. Electron.* **2018**, *65*, 4670–4680. [[CrossRef](#)]
9. Cabrera, T.; Sánchez, J.A.A.; Longo, M.; Foidelli, F. Sensitivity analysis of a bidirectional wireless charger for EV. In Proceedings of the 2016 IEEE International Conference on Renewable Energy Research and Applications (ICRERA), Birmingham, UK, 20–23 November 2016; pp. 1113–1116.
10. Zhang, Y.; Kan, T.; Yan, Z.; Mi, C.C. Frequency and Voltage Tuning of Series–Series Compensated Wireless Power Transfer System to Sustain Rated Power Under Various Conditions. *IEEE J. Emerg. Sel. Top. Power Electron.* **2019**, *7*, 1311–1317. [[CrossRef](#)]
11. Shin, J.; Outeiro, M.T.; Czarkowski, D. New real-time tuning method for wireless power transfer systems. In Proceedings of the IEEE Wireless Power Transfer Conference (WPTC), Aveiro, Portugal, 5–6 May 2016; pp. 1–4.
12. Sasatani, T.; Narusue, Y.; Kawahara, Y.; Asami, T. DC-based impedance tuning method using magnetic saturation for wireless power transfer. In Proceedings of the IEEE Wireless Power Transfer Conference (WPTC), Taipei, Taiwan, 10–20 May 2017; pp. 1–4.
13. Saltanovs, R. Multi-capacitor circuit application for the wireless energy transmission system coils resonant frequency adjustment. In Proceedings of the IEEE Wireless Power Transfer Conference (WPTC), Boulder, CO, USA, 13–15 May 2015.
14. Baikova, E.N.; Baikov, A.V.; Valtchev, S.; Melicio, R. Frequency Tuning of the Resonant Wireless Energy Transfer System. In Proceedings of the 45th Annual Conference of the IEEE Industrial Electronics Society (IECON), Lisbon, Portugal, 14–17 October 2019.
15. Xia, J.; Chen, D.; Wang, D.; Xu, D. Analysis of Automatic Frequency Tuning for Wireless Power Transfer Systems. In Proceedings of the IEEE 4th Advanced Information Technology, Electronic and Automation Control Conference (IAEAC), Chengdu, China, 20–22 December 2019.
16. Sis, S.A.; Bicakci, S. A resonance frequency tracker and source frequency tuner for inductively coupled wireless power transfer systems. In Proceedings of the 46th European Microwave Conference (EuMC), London, UK, 4–6 October 2016; pp. 751–754.
17. Kar, D.P.; Nayak, P.P.; Bhuyan, S.; Panda, S.K. Automatic frequency tuning wireless charging system for enhancement of efficiency. *Electron. Lett.* **2014**, *50*, 1868–1870. [[CrossRef](#)]
18. Wang, C.-S.; Covic, G.A.; Stielau, O.H. Power transfer capability and bifurcation phenomena of loosely coupled inductive power transfer systems. *IEEE Trans. Ind. Electron.* **2004**, *51*, 148–157. [[CrossRef](#)]
19. Chopra, S.; Bauer, P. Analysis and design considerations for a contactless power transfer system. In Proceedings of the IEEE 33rd International Telecommunications Energy Conference (INTELEC), Amsterdam, The Netherlands, 9–13 October 2011.
20. Villa, J.L.; Sallan, J.; Sanz Osorio, J.F.; Lombart, A. High-Misalignment Tolerant Compensation Topology For ICPT Systems. *IEEE Trans. Ind. Electron.* **2012**, *59*, 945–951. [[CrossRef](#)]

21. Sohn, Y.H.; Choi, B.H.; Lee, E.S.; Lim, G.C.; Cho, G.H.; Rim, C.T. General Unified Analyses of Two-Capacitor Inductive Power Transfer Systems: Equivalence of Current-Source SS and SP Compensations. *IEEE Trans. Power Electron.* **2015**, *30*, 6030–6045. [[CrossRef](#)]
22. Qu, X.; Jing, Y.; Han, H.; Wong, S.C.; Tse, C.K. Higher Order Compensation for Inductive-Power-Transfer Converters With Constant-Voltage or Constant-Current Output Combating Transformer Parameter Constraints. *IEEE Trans. Power Electron.* **2017**, *32*, 394–405. [[CrossRef](#)]
23. Aditya, K.; Williamson, S.S. A Review of Optimal Conditions for Achieving Maximum Power Output and Maximum Efficiency for a Series-Series Resonant Inductive Link. *IEEE Trans. Transport. Electrification.* **2017**, *3*, 303–311. [[CrossRef](#)]
24. Buja, G.; Bertoluzzo, M.; Mude, K.N. Design and experimentation of IPT charger for electric city car. *IEEE Trans. Ind. Electron.* **2015**, *62*, 7436–7447. [[CrossRef](#)]
25. Aditya, K.; Williamson, S.S. Design Guidelines to Avoid Bifurcation in a Series-Series Compensated Inductive Power Transfer System. *IEEE Trans. Ind. Electron.* **2019**, *66*, 3973–3982. [[CrossRef](#)]
26. CY8CKIT-059 PSoC 5LP Prototyping Kit Guide. Available online: <http://http://www.cypress.com/file/157971/download>, (accessed on 21 February 2020).
27. Mude, K.N.; Bertoluzzo, M.; Buja, G.; Pinto, R. Design and experimentation of two-coil coupling for electric city-car WPT charging. *J. Electromagn. Waves Appl.* **2016**, *30*, 70–88. [[CrossRef](#)]
28. CCS050M12CM2 1.2kV, 25mΩ All-Silicon Carbide Six-Pack (Three Phase) Module. Available online: <https://www.wolfspeed.com/ccs050m12cm2>, (accessed on 21 February 2020).



© 2020 by the authors. Licensee MDPI, Basel, Switzerland. This article is an open access article distributed under the terms and conditions of the Creative Commons Attribution (CC BY) license (<http://creativecommons.org/licenses/by/4.0/>).